# Membrane Domain Formation, Interdigitation, and Morphological Alterations Induced by the Very Long Chain Asymmetric C24:1 Ceramide

Sandra N. Pinto,* Liana C. Silva,* Rodrigo F. M. de Almeida,[†] and Manuel Prieto*

*Centro de Química-Física Molecular, Instituto Superior Técnico, 1049-001 Lisbon, Portugal; and [†]Centro de Química e Bioquímica, Faculdade de Ciências, Universidade de Lisboa, 1749-016 Lisbon, Portugal

ABSTRACT   Ceramide (Cer) is involved in the regulation of several biological processes, such as apoptosis and cell signaling. The alterations induced by Cer in the biophysical properties of membranes are thought to be one of the major routes of Cer action. To gain further knowledge about the alterations induced by Cer, membrane reorganization by the very long chain asymmetric nervonoylceramide (NCer) was studied. The application of an established fluorescence multiprobe approach, together with x-ray diffraction, differential scanning calorimetry, and confocal fluorescence microscopy, allowed the characterization of NCer and the determination of the phase diagram of palmitoyloleoylphosphatidylcholine (POPC)/NCer binary mixtures. Nervonoylceramide undergoes a transition from a mixed interdigitated gel phase to a partially interdigitated gel phase at ~20°C, and a broad main transition to the fluid phase at ~52°C. The solubility of NCer in the fluid POPC is low, driving gel-fluid phase separation, and the binary-phase diagram is characterized by multiple and large coexistence regions between the interdigitated gel phases and the fluid phase. At 37°C, the relevant phases are the fluid and the partially interdigitated gel. Moreover, the formation of NCer interdigitated gel phases leads to strong morphological alterations in the lipid vesicles, driving the formation of cochleate-type tubular structures.

## INTRODUCTION

Ceramide (Cer) has emerged as one of the most important sphingolipids, given that it is the key intermediate in the sphingomyelin (SM) synthetic pathway (1), and because it is involved in the regulation of various cellular processes such as proliferation, differentiation, apoptosis, growth, and inflammation (2).

Different processes, including tumor necrosis factor-$\alpha$ signaling, conditions known to provoke cell stress (e.g., radiation and heat), and chemotherapeutic drugs and oxidants, are inducers of Cer accumulation, as reviewed elsewhere (3,4). The major route of acute Cer formation, in addition to de novo synthesis, is the hydrolysis of sphingomyelin by the action of the enzyme sphingomyelinase (3).

The Cer N-acyl chains can vary both in length (from 14–26 carbon atoms) and in degree of unsaturation (5). The most common Cer N-acyl chains in mammalian cells are C16–C24 (6), and it was suggested that Cer with different structures participates in distinct cell functions (7). In addition, several pieces of evidence indicate a biophysical role of Cer in the modulation of biological processes, e.g., through the formation of so-called Cer platforms (8). Therefore, it is important to understand the impact of the acyl chain of Cer in the properties of a model membrane.

Several studies showed that long-chain Cer (mainly with C16 and C18) can increase the order of acyl chains of the surrounding phospholipids (9,10), permeabilize lipid bilayers (11), induce membrane fusion, fission, and transmembrane (flip-flop) lipid motion (12,13), and laterally separate in the plane of the membrane, leading to the formation of distinct Cer-rich and phospholipid-rich domains (14–18).

However, literature concerning the biophysical behavior of very long-chain Cer or mixtures of long-chain Cer (e.g., bovine brain Cer [bbCer]) is scarce (14,15,19,20). Nervonoylceramide (C24:1, NCer, Fig. 1) is a very common lipid in several mammalian tissues, presenting relatively high levels in the liver, kidney, and brain, compared with other long-chain forms of Cer (21). Nervonoylceramide has very asymmetrical hydrocarbon chains (different lengths) and an unsaturation close to the center of the longer chain (Fig. 1). It is thus plausible that NCer forms interdigitated phases because of the strong asymmetry among the acyl chain and the sphingoid base (22), which might facilitate cell-signaling through the coupling between the inner and outer membrane leaflets (23).

To understand how NCer affects the properties of a fluid membrane, the binary system palmitoyloleoylphosphatidylcholine (POPC)/NCer was characterized by fluorescence spectroscopy. Through the application of a multiprobe methodology (10), complemented by differential scanning calorimetry (DSC) and x-ray scattering, it was possible to describe the biophysical behavior of this system, and to determine its binary-phase diagram. It was shown that NCer presents low solubility in fluid POPC, leading to the formation of NCer-rich gel domains. The application of confocal fluorescence microscopy further shows the ability of NCer to segregate into gel domains with typical flower-like patterns, and to induce vesicle aggregation and tubular structure formation. Moreover, the complexity of the phase behavior and
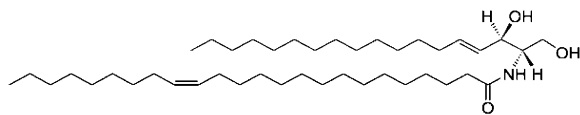
FIGURE 1    Structure of NCer.

morphology can be ascribed to the formation of multiple, interdigitated gel phases.

## MATERIALS AND METHODS

### Materials

The POPC, NCer, and *N*-rhodamine-dipalmitoylphosphatidylethanolamine (Rho-DOPE) were obtained from Avanti Polar Lipids (Alabaster, AL). The 1,6-diphenyl-1,3,5-hexatriene (DPH), 1-[4-(trimethylamino)phenyl]-6-phenylhexa-1,3,5-triene (TMA-DPH), and trans-parinaric acid (t-PnA) were from Molecular Probes (Leiden, The Netherlands). All organic solvents were UVASOL grade from Merck (Darmstadt, Germany).

### Liposome preparation

Multilamellar vesicles (MLVs) containing the adequate lipids, TMA-DPH, and DPH were prepared as previously described (10). Unless otherwise stated, the total lipid concentration used was 0.1 mM. The suspension medium contained sodium phosphate 10 mM, NaCl 150 mM, and EDTA 0.1 mM buffer (pH 7.4). Samples were re-equilibrated by freeze-thaw cycles and incubation at >90°C. For studies with t-PnA, samples were slowly brought to room temperature, and the probe was then added from an ethanol stock solution (final ethanol volume always <1%, preventing bilayer destabilization (24)). Samples were again re-equilibrated by freeze-thaw cycles and subsequently kept overnight at 4°C. Before measurements, samples were slowly brought to room temperature and maintained at this temperature for at least 1 h. The probe/lipid ratios were 1:200 for DPH, 1:150 for TMA-DPH, and 1:500 for t-PnA.

The concentration of POPC and NCer stock solutions was determined gravimetrically with a high-precision balance (Mettler Toledo UMT2 (Columbus, OH)). Probe concentrations were determined spectrophotometrically, using $\varepsilon$(t-PnA, 299.4 nm, ethanol) $= 89 \times 10^3$ $M^{-1}cm^{-1}$ (25), $\varepsilon$(DPH, 355 nm, chloroform) $= 80.6 \times 10^3$ $M^{-1}cm^{-1}$ (26), and $\varepsilon$(TMA-DPH, 355 nm, chloroform) $= 52 \times 10^3$ $M^{-1}cm^{-1}$ (determined in this study).

### Absorption and fluorescence measurements

All measurements were performed in 0.5 cm $\times$ 0.5 cm quartz cuvettes under magnetic stirring. For absorption, a Shimadzu UVPC-3100 spectrophotometer (Shimadzu, Kyoto, Japan) was used. Fluorescence steady-state measurements were performed in a SLM-Aminco 8110 Series 2 spectrofluorometer (Rochester, NY). The excitation ($\lambda_{exc}$) and emission ($\lambda_{em}$) wavelengths were: $\lambda_{exc} = 358$ nm and $\lambda_{em} = 430$ nm for DPH and TMA-DPH, and $\lambda_{exc} = 303$ nm and $\lambda_{em} = 405$ nm for t-PnA. The temperature was achieved using a Julabo F25 circulating water bath (Houston, TX), and was controlled within 0.1°C directly inside the cuvette with a type-K thermocouple (Electrical Electronic Corp., Taipei, Taiwan). The heating rate was always below 0.2°C/min.

The fluorescence-decay measurements were obtained by a single photon-timing technique. Measurements with t-PnA ($\lambda_{exc} = 295$ nm and $\lambda_{em} = 405$ nm) were performed using a secondary laser of rhodamine 6G (27). For DPH and TMA-DPH measurements ($\lambda_{exc} = 360$ nm and $\lambda_{em} = 430$ nm), a Ti-Sapphire laser was used (28). To obtain the fitting curves, experimental decays were analyzed using TRFA software (Scientific Software Technologies Center, Minsk, Belarus). Fluorescence decays were described by a sum of exponentials, where $\alpha_i$ is the normalized pre-exponential (or amplitude), and $\tau_i$ is the lifetime of the decay component $i$. The mean fluorescence lifetime $\langle \tau \rangle$ is given by $\langle \tau \rangle = \sum_i \alpha_i \tau_i^2 / \sum_i \alpha_i \tau_i$.

### Differential scanning calorimetry

For DSC measurements, MLVs with total lipid concentrations of 0.75 mM were prepared as described above. Because of the low solubility of pure Cer and mixtures containing high molar fractions of long-chain Cer (14,15,29), and the strong tendency of Cer to form nonbilayer aggregates, it was necessary to sonicate samples (Branson Sonifier 250 with a microprobe (Schäwbisch Gmünd, Germany)) to obtain stable dispersions (samples were centrifuged for 5 min at 8000 rpm to isolate titanium released from the probe tip). The DSC experiments were performed with a Microcal VP-DSC (Microcal, Northampton, MA). All mixtures were prepared 1 day before DSC measurements, and were allowed to equilibrate overnight at 4°C. Before loading into the DSC cells, both sample and buffer were degassed under a vacuum. Heating and cooling scans were run at a rate of 0.5°C/min, unless stated otherwise. Thermogram analysis was performed using software supplied with the calorimeter (ORIGIN, MicroCal), based on the Levenberg/Marquardt nonlinear least-squares fitting method. The best fit to the experimental data was obtained with the independent non-two-state transitions model, previously shown to be the best model for describing DSC data from bbCer mixtures (29).

### X-ray diffraction

For x-ray scattering measurements, MLVs with a final lipid concentration of 35 mM were prepared as described above. After liposome preparation, samples were centrifuged at 13,000 rpm for 30 min, and the pellets were stored at 4°C. To perform the measurements, the pellets were transferred to a glass capillary. Small and wide-angle x-ray scattering (SAXS and WAXS) was performed at 20°C, using a Philips X'Pert diffractometer (Warsaw, Poland), operating with a monochromatic CuK$\alpha$ radiation source at 40 kV and 50 mA, from 0.63° to 65° with 0.03° steps and a 2-s time per step.

### Confocal fluorescence microscopy

Giant unilamellar vesicles (GUVs) containing adequate lipids and Rho-DOPE ($\varepsilon$(Rho-DOPE, 559 nm, chloroform) $= 95 \times 10^3$ $M^{-1}cm^{-1}$) at a probe/lipid ratio of 1:500 were prepared by electroformation, using Pt electrodes, as described previously (30), or using Ti plates (31) separated by a tightly fitted Teflon spacer. The results obtained were essentially the same. Regarding the use of Pt electrodes, an alteration to the previous protocol was made, to improve the methodology. Briefly, we used glass tubes with plastic stoppers protected with Teflon. Two holes were machined on the stoppers, with the diameter matching the diameter of the Ag wire in the plastic outer part, and the diameter was 0.25 mm smaller than the Ag wire in the Teflon inner part, for the sake of tight accommodation with the wire. Hence, we minimized the entry of air into the tube during vesicle formation, and achieved ease of parallel positioning of the Pt tips where the lipid mixture was spread. In both the Ti capacitor and Pt electrodes, the lipids and probe were mixed in chloroform/methanol ($\sim$2:1 v/v), with a total concentration of $\sim$1 mM. The hydration medium was 200 mM sucrose in MilliQ (Billerica, MA) purified water, preheated to a temperature above the main transition temperature for the particular mixture (room temperature, 40°C, and 50°C for 5, 20, and 30 mol % NCer, respectively). The hydration medium was deoxygenated, and the GUVs formed at these hydration temperatures. After GUV formation, the temperature was slowly reduced to 22°C. Aliquots of 50 $\mu$L for the Ti plates and 150 $\mu$L for the Pt electrodes were collected and transferred to the wells of an eight-well plastic plate with a coverslip-like bottom. To settle the GUVs to the bottom of the chamber, a difference in the density between the solutions inside and outside the vesicles was created by adding 300 or 200 $\mu$L of 200 mM glucose solution in MilliQ water to the aliquots.

Microscopy was performed with a Leica TCS SP5 (Leica Mycrosystems CMS GmbH, Mannheim, Germany) inverted microscope (DMI6000) with a 63$\times$ water (1.2 numerical aperture) apochromatic objective. Before turning to the confocal mode, the GUV suspension was directly observed using a sodium lamp as the light source, and using a filter to select Rho-DOPE fluorescence, to evaluate the yield of GUV formation and the homogeneity of

the suspension, in terms of size, morphology, and fluorescence intensity. The GUV yield was very high for the lowest Cer fraction, and decreased with increasing Cer content, a trend also observed for average GUV size, as previously verified in systems containing other long-chain Cer and nervonoyl-PC (32,33). The GUVs had similar maximum intensity within a sample, showing a homogeneous probe distribution, and between samples of similar or different composition, in agreement with the expected presence of a similar POPC-enriched fluid phase in all samples.

For confocal fluorescence microscopy, excitation was performed with the 514-nm line from an $Ar^+$ laser. The emission was collected from 550–680 nm, i.e., practically all the emission was collected, and at the same time, photons with wavelengths where emission did not occur were not reaching the detector, taking advantage of the acoustic-optical tunable fiber and beam splitter of the Leica TCS SPC5 system. The laser power and the gain of the photomultiplier tube detector were similar in all samples, further showing homogeneous probe distribution and similar fluid phase in all observed GUVs. Stray light was minimized, in accordance with a ''smart offset'' always below 0.5%, and photon counts outside the lipid structures were negligible. Confocal sections of thickness below 0.5 $\mu$m were obtained using the galvanometric motor stage. Three-dimensional (3D) projections were obtained using Leica Application Suite-Advanced Fluorescence software.

## RESULTS

### Thermotropic characterization of NCer and POPC/NCer mixtures by fluorescence spectroscopy

To determine the thermotropic behavior of fully hydrated NCer, the steady-state fluorescence anisotropy of different probes (incorporated in NCer membranes) was measured as a function of temperature (Fig. 2 A). It was observed that TMA-DPH anisotropy is very high and typical of a gel phase in the low temperature range, and upon increasing the temperature above 40°C, there is a sharp decrease in the anisotropy of the probe, down to values typical of a fluid phase. This variation is attributable to the transition from the gel to the fluid phase of NCer, and from these data, the main transition temperature ($T_m$) of the lipid was determined. Briefly, the $T_m$ of ~52°C was taken as the midpoint of intersection of the lines describing the initial (gel), intermediate, and final (fluid) regimes. In addition to the main transition, it is also possible to distinguish a smaller transition at ~20°C. This pretransition

is probably an interconversion between two interdigitated gel states, as previously observed for other asymmetric lipids, e.g., N-lignoceroylsphingosylphosphocholine (34), leading to only a slight variation of the parameter under observation ~30°C below $T_m$.

Neither DPH (data not shown) nor t-PnA is able to report the gel-fluid phase transition, because the probes are excluded from the membrane because of the formation of a highly compact NCer gel. Although DPH and TMA-DPH present the same chromophore, TMA-DPH is not excluded from the membrane because of the presence of the cationic trimethylamonium group, which anchors the probe to the membrane surface.

Fig. 2 B shows the anisotropy of t-PnA, TMA-DPH, and DPH in POPC as a function of temperature. This lipid is fluid in the temperature range of this study ($T_m = -2.9 \pm 1.3$°C (35)), and therefore the observed decrease in anisotropy is attributable only to a gradual increase of membrane fluidity with temperature, and is not associated with a phase transition. In the presence of 10% NCer (Fig. 2 C), t-PnA can detect NCer-induced changes in fluid POPC. At 4°C, t-PnA anisotropy is higher than in POPC, and in addition, an inflection is observed in the curve, suggesting the presence of NCer-enriched gel domains. Slightly increasing the temperature leads to an abrupt decrease in t-PnA anisotropy down to values similar to those obtained in pure POPC, reflecting a transition from the gel to the fluid phase, which ends at ~24°C. In this mixture, TMA-DPH and DPH anisotropy have values and a trend of variation identical to what was observed in POPC, showing that these probes are unable to detect the presence of NCer-gel domains. With 50% NCer (Fig. 2 D), DPH fluorescence anisotropy values are lower than those typical of a gel phase (e.g., 0.3 in POPC/SM mixtures (27)), and this probe remains unable to report the gel-fluid phase transition. In contrast, t-PNA and TMA-DPH present clearly different regimes. It should be stressed that the attachment of the TMA group to DPH confers an additional restriction to the rotational diffusion of the chromophore, leading to a higher intrinsic anisotropy in the fluid phase (Fig.
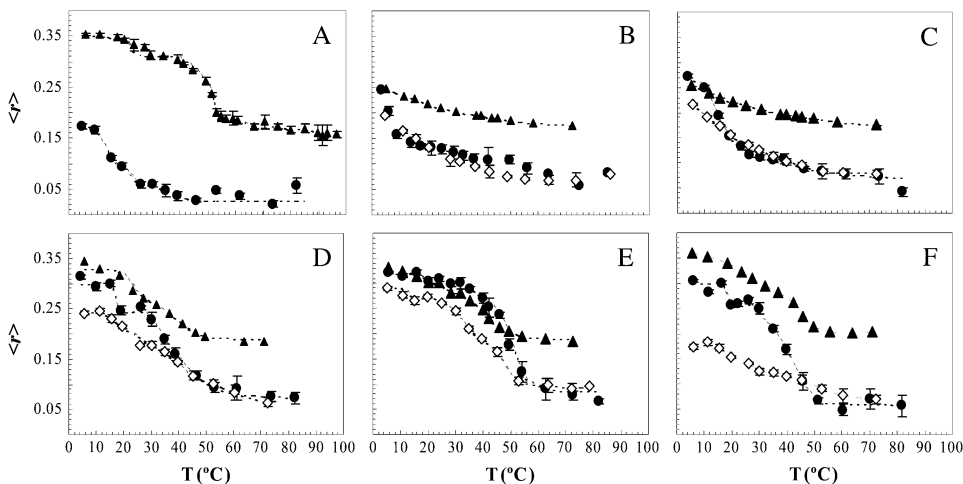


FIGURE 2 Thermotropic behavior of POPC/NCer. Steady-state fluorescence anisotropy of t-PNA ($\bullet$), DPH ($\diamond$), and TMA-DPH ($\blacktriangle$) as a function of temperature (T) in MLV composed of (A) NCer, (B) POPC, and POPC/NCer mixtures containing (C) 10% NCer, (D) 50% NCer, (E) 70% NCer, and (F) 80% NCer. Dashed lines are given as visual aids. Values are the averages of three independent experiments.

2 *B*). As a consequence, the difference between the anisotropy values of TMA-DPH in the gel and fluid phase is not as large as the difference observed for t-PnA. For 70% NCer (Fig. 2 *E*), all probes presented an anisotropy profile of variation typical of a gel-fluid phase transition. However, increasing NCer to 80% leads to the exclusion of DPH (Fig. 2 *F*), and only t-PnA and TMA-DPH are able to report the thermotropic behavior of this mixture.

Similar to 100% NCer, the mixtures containing more than 50% NCer also present a smaller transition at ~20°C, as detected by TMA-DPH and t-PnA (Fig. 2, *A*, *D*, *E*, and *F*), and corresponding to a transition between interdigitated gel phases.

The temperatures at which the system became 100% fluid ($T_f$), as determined using the different probes (in cases where the transition was detected), were identical, and comprised the starting point for building up a binary-phase diagram (see Discussion).

## Thermotropic characterization of NCer and POPC/NCer mixtures by DSC

To obtain additional information regarding the thermotropic behavior of the system under study, DSC was performed for the NCer and POPC/NCer binary mixtures. Representative heating scans of these samples are shown in Fig. 3. Nervonoylceramide presents a broad endothermic peak centered at ~52°C, coincident with the transition reported by TMA-DPH anisotropy. Because of the complex nature of the main endotherm (very broad, asymmetric, and with a low signal/noise ratio), it was not possible to determine with accuracy the enthalpy of the main transition. In addition to the main peak, a small endothermic peak (~20°C) and a shoulder at higher temperatures (~70°C) were also detected (Fig. 3). The pretransition is attributable to the conversion between interdigitated gel phases, and the highest temperature transition can be ascribed to a conversion to a nonlamellar phase, as suggested for other long-chain Cer (29).

Regarding the binary mixtures, for those containing 5% NCer, no transition was detected in the temperature range studied. For mixtures containing more NCer, an endothermic peak, corresponding to a gel-fluid phase transition, was present in the thermogram. Furthermore, with increasing NCer content, it is clear that: 1), the transition temperature is shifted toward higher values; and 2), the main endotherm becomes broader, i.e., the temperature width at half-maximum increases, and becomes more asymmetric. In addition, the pretransition becomes clear with increasing NCer amounts, as evidenced by the presence of a small peak for mixtures containing NCer ≥70%.

## Defining the lipid phases

Fig. 4 *A* shows the fluorescence anisotropy of the three probes as a function of NCer mole fraction ($X_{NCer}$) at room tem-
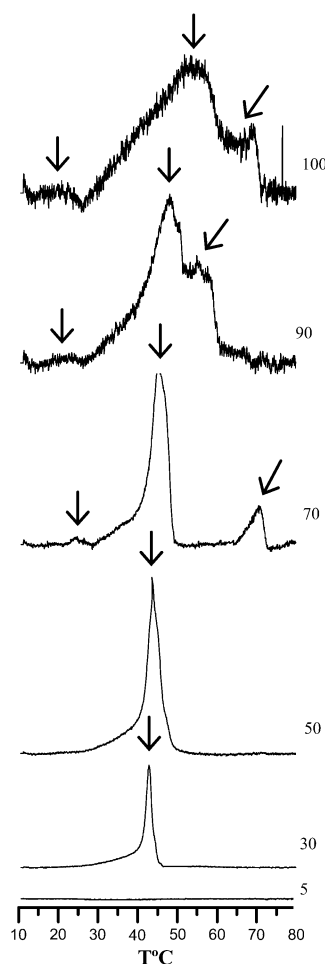


FIGURE 3   DSC thermograms of NCer and POPC/NCer mixtures. The *y*-scales were adjusted to better define the spectral characteristics of each sample. Arrows indicate the main transition (gel-fluid phase transition) and, for the highest NCer mol fraction, the transition between interdigitated gel phases (pretransition at ~20°C). See text for further details. *T*, temperature.

perature (24°C). The t-PnA anisotropy presents a sharp increase for $X_{NCer} > 10\%$, reaching a plateau between 50–70% NCer. These high anisotropy values are typical of the Cer gel phase (10). For higher NCer concentrations, t-PnA anisotropy decreases, showing that the probe is excluded from the membrane because of the formation of a highly compact gel phase, similar to the one reported for palmitoyl-Cer (PCer) (10). The t-PnA fluorescence excitation spectra in mixtures containing NCer ≥70–80% also present the excitonic spectral alterations (data not shown) typical of the formation of probe micelles in water (36). Thus the variation profile of t-PnA anisotropy allows us to distinguish between three regimes:1), a fluid phase, up to 10% NCer; 2), a gel-fluid phase coexistence region, up to 70% NCer; and 3), a highly ordered gel phase for $X_{NCer}$ higher than ~70%. Using TMA-DPH as a probe, it is also possible to distinguish these three regimes: up to 10% NCer, TMA-DPH anisotropy is constant and typical of a fluid phase; upon increasing the NCer concentration, the anisotropy of the probe increases linearly up to 70% NCer,
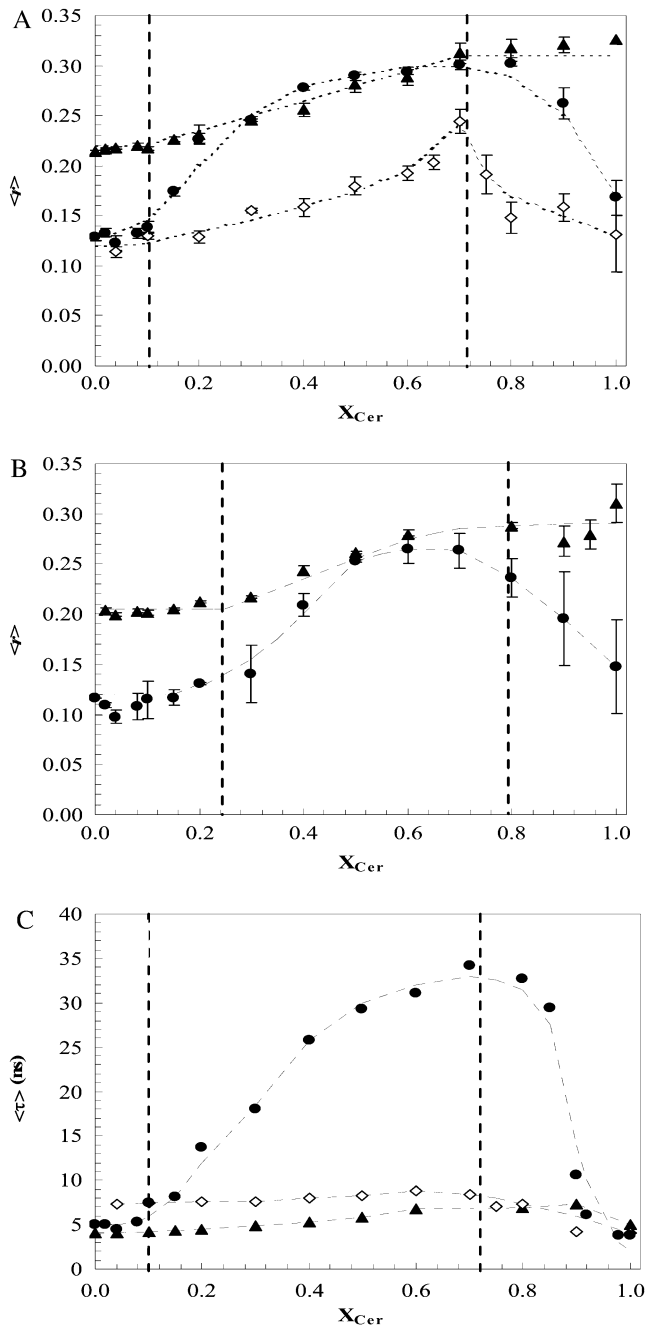
FIGURE 4 Steady-state fluorescence anisotropy (*A* and *B*) and mean fluorescence lifetime (*C*) of t-PNA (●), DPH (◇), and TMA-DPH (▲), in POPC/NCer binary mixtures at (*A* and *C*) 24°C and (*B*) 37°C. Vertical dashed lines correspond to gel and fluid phase boundaries. Dotted lines are given as visual aids. Values are the averages of three independent experiments. In *C*, the error bars are smaller than the size of the symbol.

remaining constant and with values typical of gel phase until 100% NCer is reached. Similar anisotropy profiles of variation were observed for t-PnA and TMA-DPH at 37°C (Fig. 4 *B*), demonstrating once again the existence of the three regimes: fluid phase up to ~25%, gel-fluid phase coexistence from ~25–80%, and gel. For DPH, the anisotropy trend of variation

is completely different. The anisotropy of the probe remains low, presenting a slight increase with NCer content. For 70% NCer, DPH anisotropy increases up to a value of 0.23, indicating that the probe is not completely excluded from the NCer-gel phase, but has a very low partition into it. Only when the gel phase approaches 100% inside the coexistence region is DPH able to report the presence of that phase. It should be stressed that this was the only mixture studied for which DPH was able to detect the gel-fluid phase transition (Fig. 2 *E*). Above this Cer content, DPH anisotropy decreases, because of the exclusion of the probe from the membrane, meaning that a phase boundary at 24°C must be very close to $X_{NCer} \sim 0.7$.

Fig. 4 *C* shows the mean fluorescence lifetimes of the probes in POPC/NCer mixtures as a function of $X_{NCer}$ at 24°C. For t-PnA, the profile of variation is similar to that observed for anisotropy (Fig. 4 *A*), further showing the presence of the three regimes, i.e., fluid, gel + fluid, and gel. Also, the longer mean fluorescence lifetime values are unique to the gel phase (25), undoubtedly confirming the presence of the NCer-rich gel phase. It should be stressed that the increase in anisotropy is not attributable to a decrease in fluorescence lifetime (according to the Perrin equation (37)), and, therefore, the profiles of variation of both anisotropy fluorescence lifetimes strongly support the presence of a highly ordered environment in the vicinity of the probe.

The variation in fluorescence lifetimes observed for both TMA-DPH and DPH is less steep than for t-PnA. The dependence of the fluorescence lifetime of these probes on the lipid phase is small (38). Once again, the absence of a strong decrease in the fluorescence lifetime of the probes confirms that the increase in anisotropy is attributable to an increase in the order of the membrane, validating the conclusions derived from the anisotropy data.

## X-ray scattering of NCer and NCer/ POPC mixtures

Both SAXS and WAXS were used to obtain further structural information on the types of phases formed by NCer and NCer/ POPC mixtures (Fig. 5). A single reflection was observed at 4.2 Å in the wide-angle region for mixtures containing 20–60% NCer, typical of a lamellar gel phase with hexagonal packing (39,40). For 5% and 10% NCer, this reflection appeared as a broader peak, with the maximum shifted to 4.3 Å and a shoulder at ~4.5 Å, because of the contribution of the fluid phase. Increasing NCer to 80% and 90%, the peak split into two (Fig. 5, *A* and *C*), with the appearance of an additional reflection at 3.9 Å, revealing the presence of two gel phases (41).

The SAXS diffractograms showed a single and symmetric peak, with a repeat distance that increased with NCer content up to 50%. Upon increasing NCer to 80%, the first-order diffractions became broader and asymmetric, with a maximum at ~58 Å, and a shoulder at longer distances (~65 Å). For pure NCer, the SAXS diffractogram presented a single broad and asymmetric peak at ~57 Å.
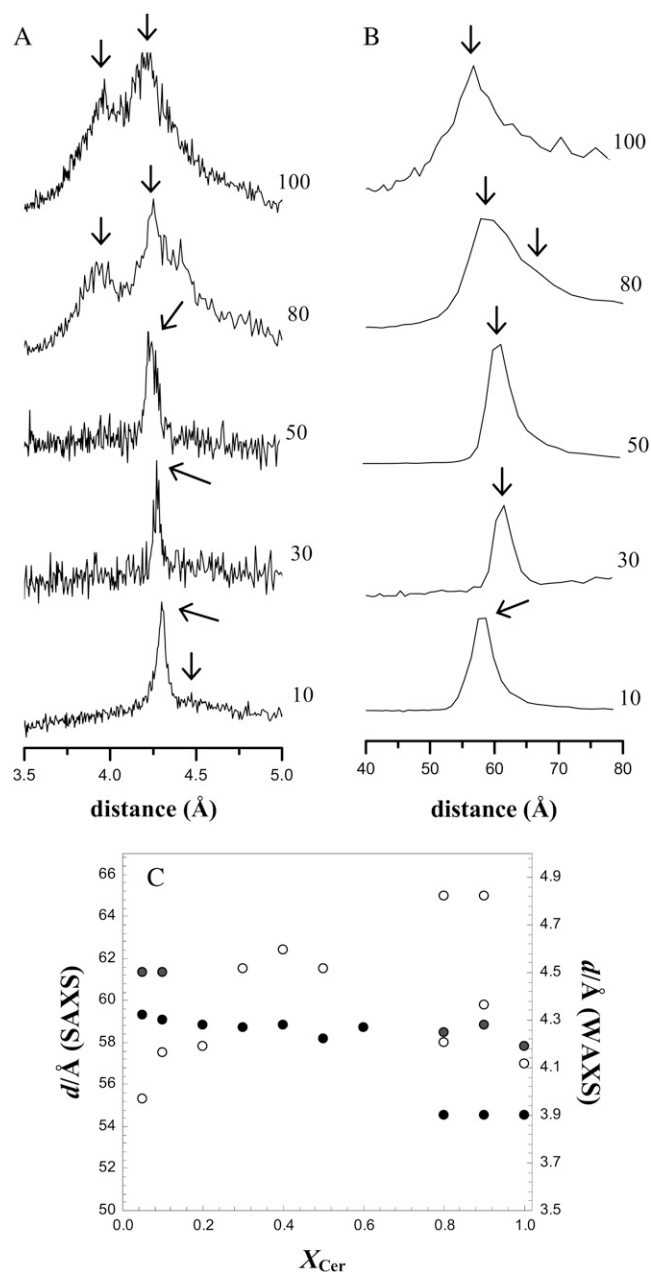
FIGURE 5  Wide-angle (*A*) and small-angle (*B*) x-ray scattering spectra of NCer and POPC/NCer mixtures. The *y*-scales were adjusted to better define the spectral characteristics of each sample. (*C*) Wide-angle (*solid circles*) and small-angle (*open circles*) reflections as a function of NCer content. Beside the main reflection (both in WAXS and SAXS), additional reflections are shown, when detected, for a particular mixture.

## Observation of micron-scale gel/fluid phase separation in NCer containing GUVs

To characterize further the biophysical properties of POPC/NCer mixtures, confocal fluorescence microscopy was performed on GUVs (Fig. 6) at 22°C. The probe used for this purpose was Rho-DOPE because of its absorption and emission in the visible range, photostability, high molar ab-

sorption coefficient and quantum yield, and known gel-fluid partition coefficient in a mixture of saturated and unsaturated PC. The quantum yield of the probe is similar in gel and fluid phases for probe concentrations <0.5 mol %, but the partition is highly unfavorable for the gel phase (30). In this way, gel/fluid-phase separation should be easily observed in GUVs, as bright (fluid) and dark (gel) domains.

In Fig. 6 *A*, a 3D projection of confocal slices of POPC/NCer (95:5 mol/mol) GUV is shown. As observed for all GUVs with this composition, no domains are present, in agreement with fluorescence spectroscopy and DSC results. However, increasing the NCer concentration to 20 mol % (Fig. 6 *B*) leads to the appearance of micron-sized domains. The dark domains, because of their lower brightness and nonround shape, are undoubtedly gel (Cer-enriched) domains (30). Increasing the NCer content further to 30 mol % (Fig. 6 *C*), the dark domains are larger, exhibiting a clear flower-like pattern. The gel-domain surface-area fraction is higher than for the previous composition, as expected for higher Cer content, and again in agreement with fluorescence spectroscopy data (e.g., Fig. 4).

In addition to the vesicles with clearly defined gel domains, for 20 and 30 mol % NCer, aggregated vesicles, and mixed vesicle-tubular and tubular structures, were also observed. The 3D projections of confocal slices of representative structures are shown in Fig. 6, *D–F*. The number and complexity of this kind of structure are larger for 30% NCer (Fig. 6 *F*), suggesting a direct relationship with composition/phase behavior.

## DISCUSSION

### Thermotropic behavior of NCer and properties of phases

Regarding NCer and mixtures containing NCer, little is known about their phase behavior and the structures formed. To our knowledge, only one work reported on the properties of monolayers containing NCer (19), whereas other studies focused on the effects of bovine or porcine brain Cer mixed with different lipids (14,15,20,29,42). For a better definition of NCer properties and effects on membrane biophysics, DSC and X-ray diffraction were used to complement fluorescence spectroscopy and microscopy, keeping in mind the shortcomings of each technique.

Fluorescence anisotropy (Fig. 2 *A*) and DSC (Fig. 3) showed that the gel-to-fluid phase transition of NCer occurs in a broad range of temperatures, and at relatively low values (Figs. 2 *A* and 3), compared with other long-chain Cer, e.g., PCer and SCer ($T_m \sim 90°C$) (43,44). The difference between the $T_m$ of these Cer can be explained by the presence of one unsaturation in the NCer acyl chain, i.e., a *cis* double bond between carbon atoms 15 and 16. Considering, for example, SM, the introduction of a double bond into position 15 of the 24-carbon acyl chain has the similar effect of decreasing the saturated acyl chain length to 14 carbons in regard to the resulting $T_m$ ($T_m \sim 25°C$ for 14:0 SM, ~40.5°C for 16:0 SM, and ~23–26°C for C24:1 SM (45,46)). Structurally, the
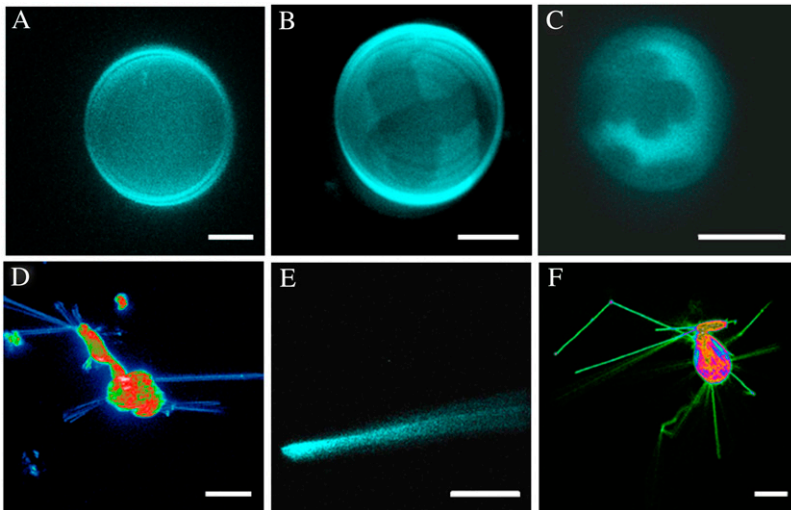
FIGURE 6 Confocal fluorescence microscopy of NCer/POPC mixtures, to observe gel domains and morphological alterations induced by NCer: 3D projection images obtained from 0.4-$\mu$m confocal slices of POPC/NCer GUV labeled with Rho-DOPE (0.2 mol %) equilibrated at 22°C. The GUVs were prepared from mixtures of POPC/NCer containing (*A*) 5%, (*B*) 20%, and (*C*) 30% NCer. Mixed vesicle-tubular and cochleate structures were observed for (*D* and *E*) 20% NCer and (*F*) 30% NCer, respectively. Scale bars correspond to 10 $\mu$m.

magnitude of the effect is dependent on the position of the double bond in the chain, and the maximal effect is observed when the *cis* double bond is in the middle of the chain (47). The *cis* double bond strongly perturbs the packing of the chains in the gel state, and therefore reduces $T_m$. Thus, sphingolipids with saturated acyl chains are more tightly packed and ordered than their monounsaturated counterparts (48). Note that the introduction of a double bond in galactosyl (Gal)-24:0 Cer leads to a decrease in $T_m$ from 84°C to 59°C (46). The thermotropic behavior of the lipids is dependent not only on the acyl chain, but also on the polar headgroup, explaining the high difference in melting temperature of 24:1 SM and NCer (49,50). Nevertheless, it was previously shown that the thermotropic behavior of PCer and the corresponding glycosphingolipids glucosyl-PCer and Gal-PCer was similar, presenting multiple phase transitions and a high melting temperature (51). For these lipids it was also shown that phase behavior was strongly influenced by the acyl chain, but was highly insensitive to the presence and type of sugar moiety (43,51). Therefore, a similarity in the thermotropic behavior of NCer and Gal-NCer can be anticipated. The $T_m$ determined in this study is comparable to the $T_m$ reported for Gal-NCer ($T_m \sim$ 59–64°C (46)). Furthermore, DSC scans showed that this glycosphingolipid presents multiple phase transitions (46). The same pattern was also observed in NCer DSC thermograms (Fig. 3): a broad main peak, with a prominent shoulder at higher temperatures. In addition, the fairly large range of temperatures for the main phase transition observed for NCer can be also attributed to an intrinsically less cooperative transition. This is commonly observed in phospholipids with asymmetric acyl chains (22).

Based on fluorescence anisotropy variation as a function of temperature (Fig. 2 *A*) and DSC scans (Fig. 3), it is possible to detect a pretransition which is attributable to the conversion between mixed and partial interdigitated gel phases, as reported for the asymmetric C24:0 SM and several binary mixtures of phospholipids with asymmetric Cer or cerebrosides (34,52).

Using vibrational Raman spectroscopy, Levin et al. (34) showed that for C24:0 SM, the first endothermic low-enthalpy transition observed in DSC thermograms was attributable to the conversion between mixed and partial interdigitated gel phases, whereas the high-enthalpy peak (second endotherm) was ascribed to the transition from the partial interdigitated gel to the fluid phase. In the mixed interdigitated gel phase, the longest chain completely interdigitates into the other leaflet, allowing an end-to-end contact between the smaller chains of the two leaflets of the membrane (see Fig. 7). The presence of other phospholipids tends to destabilize this interdigitated gel phase, and to promote a rearrangement of lipids into a more stable interdigitated gel phase, i.e., the partial interdigitated gel phase. In this phase, the longest chains partially interdigitate into the other leaflet, making end-to-end contact with the smaller chains (see Fig. 7) (34).

Further evidence for the formation of interdigitated gel phases was obtained by x-ray diffraction. A split peak with two sharp reflections at 3.9 and 4.2 Å was observed in the wide-angle region (Fig. 5 *A*). The value at 4.2 Å is very close to the value reported by Lewis et al. (40), in a study of a very large number of asymmetric cholines. This reflection was attributed to a hexagonal packing of mixed-interdigitated gel phases. Interestingly, another reflection was also present in the range of 3.7–3.9 Å, such as was observed in this work (at 3.9 Å), for pure NCer. The existence of a lamellar interdigitated gel phase with hexagonal chain packing was also suggested for C24:0 Gal-Cer, which presents a reflection at 4.2 Å in WAXS (53).

The repeat distance obtained for NCer in the small-angle region (Fig. 5 *B*) is shorter compared with the above-mentioned repeat distance for C24:0 Gal-Cer (53), where a value of 65.4 Å was reported for the interdigitated gel phase. However, this lipid contains a saturated chain and a bulky headgroup, and it is likely that this distance could be shortened in the case of the C24:1 Cer under study. Takahashi et al. (54) showed that C24:0 SM can form a mixed inter-
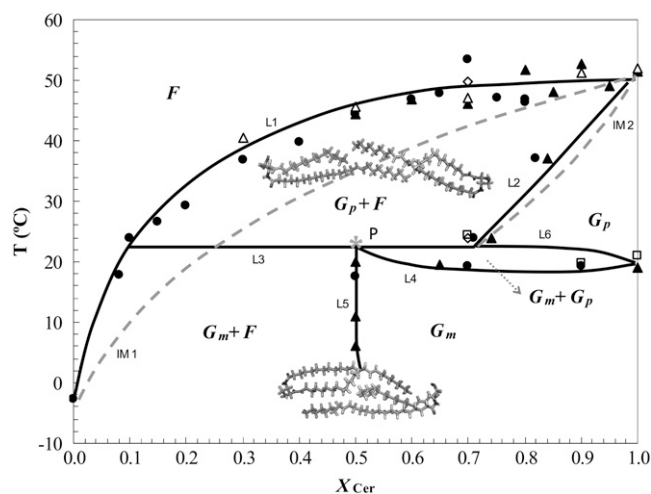
FIGURE 7 Binary-phase diagram of POPC/NCer. Solid lines were experimentally determined through the combination of fluorescence parameters of t-PNA (●), DPH (◇), and TMA-DPH (▲), whereas DSC was used to determine L1 (△), L4, and L6 (□). Confocal fluorescence microscopy was used for the determination of L3. We used x-ray scattering to validate L4, L5, and L6 and the coexistence region defined by these boundaries. See text for more details. Abbreviations: $F$, fluid phase; $G_m$, mixed interdigitated gel phase; $G_p$, partially interdigitated gel phase; $P$, peritectic point. Dashed and dotted lines were calculated assuming ideal mixing of POPC and NCer, using $\Delta H_{POPC} = 5.8$ Kcal/mol (35) and $\Delta H_{Gal\text{-}NCer} = 7$ Kcal/mol (46). IM 1 and IM 2 are, respectively, liquidus and solidus boundaries for an ideal mixture. The structures depicted in the figure correspond to the interdigitated gel phases formed by NCer.

digitated gel phase with a repeat distance of 56.2 Å. Therefore, a value of 57 Å, as obtained for NCer, is within the range of values reported for other (glyco)sphingolipids with interdigitation.

In addition to the data presented above, it is interesting to analyze the so-called chain equivalence parameter ($\Delta C/CL$), where the two variables are related to the length difference between the two chains ($\Delta C$) and the total length of the longer one ($CL$) (55), and that predicts the ability of asymmetric lipids to form interdigitated phases. According to the authors, a ratio ranging from 0.44–0.57 is typical of mixed interdigitated gel phases (56), although Lewis et al. (40) showed that some PCs whose $\Delta C/CL$ ratios were not in the defined range were able to form mixed interdigitated gel phases (40). For NCer, $\Delta C/CL = 0.41$, i.e., a value consistent with a change from a partial interdigitated to a mixed interdigitated gel phase (57).

Altogether, the results show that NCer is able to form multiple interdigitated gel phases.

## Microdomains in GUVs and other morphologies formed by POPC/NCer mixtures

Confocal fluorescence microscopy in giant vesicles allowed the direct observation of NCer-enriched domains. These domains present a flower-like pattern (i.e., they are not round),

and are micrometer-sized, as expected in the case of gel/fluid-phase separation (30).

For the lowest NCer concentration used, no gel domains were observed (Fig. 6 A), and the fraction of gel phase increased abruptly when NCer content was raised from 20 to 30 mol %. In fact, for 20 mol % NCer (Fig. 6 B), the contrast between dark and bright domains was lower than for 30 mol % NCer (Fig. 6 C). However, in the gel and fluid domains observed in GUVs with 20% and 30% NCer, it is expected that the probe concentration ratio in the two phases (partition coefficient) and the properties are the same. Indeed, for the 30 mol % NCer GUV, the gel domains are present throughout most of the surface area, and in the 3D projection, gel domains on one face of the sphere overlap with gel domains on the other face, whereas for the 20 mol % NCer GUV, they most frequently overlap with fluid domains, leading to intermediate brightness, a consequence of the 3D projection data treatment. If the hemispheres are projected (not shown), the intensity ratio of dark/bright is the same for both compositions. In addition, the huge difference in gel-phase fraction between the two mixtures suggests that close to 22°C, the tie-line should end at ~50 mol % of NCer. This implies that other phases and phase coexistence regions should be present in the POPC/NCer phase diagram for high $X_{NCer}$. It was previously shown that NCer can induce domains with a flower-like pattern in DMPC monolayers (19). Using fluorescence microscopy, the authors (19) showed that 70% NCer induced domain formation at all surface pressures, but with 20% NCer, no domains were formed at low surface pressure.

The complexity in phase behavior of NCer is further evidenced by the ability of relatively low $X_{NCer}$ (20% and 30%) to form aggregates and tubular structures (Fig. 6, D–F). We did not observe these structures in other POPC/long-chain Cer binary mixtures, using the same preparation protocol (S. Pinto, unpublished observations). It is interesting that these tubules segregate from the vesicles (Fig. 6, D and F), showing that the arrangement of NCer in the form of vesicles is unstable. This is likely attributable to the coexistence of the fluid and the interdigitated gel that leads to strong perturbations in the packing between adjacent lipids, which together with the small headgroup of NCer may induce curvature stress incompatible with GUV morphology. Therefore, the lipids in the gel phase have a high tendency to bud out of the vesicles in the form of tubules. Despite the low partition of Rho-DOPE into gel domains (30), and in particular into Cer-gel domains (17), as also shown by the contrast between dark and bright domains in GUVs (Fig. 6, B and C), it was still possible to visualize the tubules with a relatively high intensity. This suggests that these structures are cochleate in nature, formed by rolling up the bilayer. In this situation, the fairly high fluorescence intensity observed in these structures is attributable to the overlap of several membrane layers. This type of structures was observed via transmission electron microscopy for pure NCer (58,59) and other long-chain (glyco)sphingolipids (46,59). The fact that these structures were observed for 20% NCer

suggests that in vivo, where Cer can attain high local concentrations (60), the confined formation of this lipid in the cell membrane can lead to strong, local morphological alterations.

## Characteristics of phases formed by POPC/NCer mixtures

The use of several biophysical techniques proved to be a major advantage when studying complex POPC/NCer mixtures. From the thermotropic point of view, the results obtained from fluorescence spectroscopy and DSC studies provided complementary information (Figs. 2 and 3). On the other hand, fluorescence spectroscopy, x-ray diffraction, and microscopy together gave structural information, allowing the correct assignment of phases (Figs. 4–6).

From the data above, it is clear that NCer is able to induce gel-fluid phase separation. At 37°C, ~25% NCer is required to induce phase separation, whereas ~10% is enough to drive NCer-rich gel phase formation at 24°C. These results are comparable to those previously reported for POPC/porcine brain Cer mixtures (42) and DMPC/bbCer above DMPC $T_m$ (15).

Also of interest is the high rigidity of NCer gel when compared with other gel phases. For instance, NCer gel is able to exclude DPH (Fig. 4), whereas SM gel can accommodate this probe (27). However, compared with PCer, NCer gel is less rigid, because the probe is not completely excluded, as is the case with PCer (10). This difference is most likely related to the fact that at 24°C, the usual gel phase is formed in the case of PCer, whereas a partial interdigitated gel phase forms with NCer.

Overall, the data support the ability of NCer to form interdigitated gel phases, both by itself and when in lipid mixtures, e.g., in the presence of pretransitions both in fluorescence anisotropy temperature scans (Fig. 2) and DSC thermograms (Fig. 3). The presence of other phospholipids tends to destabilize the mixed interdigitated gel phase, and induce the formation of a partial interdigitated gel phase (34).

As observed for pure NCer, x-ray diffraction shows that POPC/NCer mixtures also form lamellar phases whose characteristics are dependent on NCer content. From examination of the wide-angle region, it is clear that up to 10% NCer, there is a contribution from a fluid phase, because the reflection is broader, spanning up to 4.7 Å, with a maximum shifted to ~4.3 Å (Fig 5, *A* and *C*). Increasing the NCer up to 60%, a single reflection was observed ~4.2 Å, undoubtedly confirming the presence of a gel phase. An additional weaker reflection at 3.9 Å was obtained for the 80% and 90% NCer mixtures. This shows that up to 60% NCer at the temperature of x-ray scattering measurements, one gel phase is present, and that for higher NCer fractions, two gel phases are formed. As a corollary, the x-ray diffraction was performed at a temperature very close to $T_p$ because in the pure NCer, both phases were detected. From the small-angle region, an interesting pattern of variation is obtained (Fig. 5, *B* and *C*): 1),

for the lowest NCer concentrations, the repeat distance, $d$, is shorter and in the range of the repeat distance reported for POPC (57.4 Å (61)), showing the contribution of the fluid phase, in agreement with WAXS results; 2), $d$ increases slightly with NCer (up to 50%), and this variation is consistent with DSC and spectroscopic data, showing that at this concentration, a gel phase is present. Taking into account that a higher increase in $d$ is expected when passing from a fluid to a gel phase (62), and all the more when the molecule involved in this phase formation presents a long chain, the small increase in $d$ can be explained if an interdigitated phase is being formed. Also, comparing this value with those reported, e.g., for the DPPC gel ($d \sim 66$ Å), DPPC/bbCer mixtures ($d \sim 71$ Å gel phase) (20), and DMPC/PCer mixtures ($d \geq 60$ Å, both in the fluid and in the gel) (16), it is clear that $d$ for POPC/NCer mixtures is much smaller, and therefore ascribed to interdigitation; and 3), for higher NCer concentrations, the maximum of the peak is shifted toward lower values ($d \sim 58$ Å), close to the value obtained for pure NCer. In addition, for the highest NCer concentrations (80–90%), this peak is also very broad and asymmetric, showing the coexistence of different phases. In fact, the decomposition of the peak clearly shows the presence of two populations, which can be ascribed to gel phases with different degrees of interdigitation.

## POPC/NCer binary-phase diagram

For the pure lipids POPC and NCer, the main transition temperature was taken from Koynova and Caffrey (35) and Figs. 2 *A* and 3, respectively. The pretransition observed for NCer ($T_p \sim 20$°C) is attributable to the conversion between two interdigitated gel phases, i.e., the mixed interdigitated gel phase, $G_m$, and the partial interdigitated gel phase, $G_p$. Therefore, below $T_p$, NCer is in the $G_m$ phase, and presents a transition into $G_p$ phase when $T > T_p$.

Based on anisotropy variation as a function of temperature (Fig. 2), it is possible to determine the end of the melting of gel domains and thus the $G_p +$ fluid-to-fluid ($G_p + F$-to-$F$) phase transition (liquidus boundary, L1 in Fig. 7). The points in L1 correspond to the temperature value for the end of the transition for each of the mixtures. These values were then corrected for the width of the transition of the pure lipids, according to Mabrey and Sturtevant (63). For the lower NCer concentrations, the main transition was detected by the fluorescence properties of t-PnA (Fig. 2 *C*), because of the higher preference of the probe for the gel phase. For NCer concentrations up to 80%, t-PnA and TMA-DPH data (Fig. 2, *D–F*) gave similar results with respect to the transition between the gel and fluid phases. For 70% NCer, DPH was also used for the determination of L1, confirming the transition temperature obtained with the other two probes. For very high NCer content (>90%), TMA-DPH was essential for the determination of L1, because it was the only probe that was not excluded from the highly ordered NCer-gel phase, as explained above. The DSC experiments further confirmed

the $G_p + F$-to-$F$ transition temperature of the mixtures. The values determined by DSC (Fig. 3) are very similar to those obtained by fluorescence (Fig. 7).

The $G_p + F$-to-$G_p$ phase boundary (*solid line*, *L2*, Fig. 7) was determined by both the decrease in anisotropy values and fluorescence lifetime of t-PnA because of the exclusion of the probe from the membrane (Fig. 4). This was further confirmed by the fluorescence excitation spectra of that probe, where the appearance of an excitonic interaction strongly supports this conclusion (data not shown). The profile of variation of TMA-DPH anisotropy as a function of NCer content (Fig. 4) also validates the position of the solidus boundary, because the anisotropy of the probe reaches a plateau for NCer concentrations close to those that define the boundary. In addition, DPH anisotropy variation clearly shows that a 100% $G_m$ phase is attained for ~70% NCer at 24°C.

To unravel the complexity of the low-temperature region of the diagram (Fig. 7), it was necessary to combine the results of fluorescence experiments and confocal microscopy. The analysis of the variation of the area covered by gel domains in GUVs when increasing the NCer content (Fig. 6) showed that 100% of gel should be attained at ~50% NCer (as mentioned above). Microscopy experiments were performed at 22°C, very close to the $G_m$-to-$G_p$ phase transition of NCer. The complex morphological behavior observed, with the coexistence of gel and fluid domains in GUV together with NCer-enriched tubular structures, indicates that a three-phase line must exist in the phase diagram at this temperature. Because of the shape of the liquidus boundary (L1) that spans the diagram between 0–100% NCer, the phase diagram must be of the peritectic type, i.e., presenting a horizontal line with a peritectic point (point $P$, Fig. 7), where a transition of Gel I + F to Gel II + F ($G_m$ and $G_p$, respectively) happens. In this peritectic line (*L3*, Fig. 7), all three phases are stable. If the phase diagram was of the monotectic type, then two liquidus boundaries converging at the monotectic point would have to exist, which is not the case.

Based on the anisotropy variation with temperature (Fig. 2, *D–F*), it was possible to determine $T_p$ for mixtures containing $X_{NCer} > 50\%$ (*L4*, Fig. 7). For mixtures with lower NCer content, the pretransition was not detected because of the variation in the anisotropy is broader. This difference is caused by the presence of fluid below 20°C and $X_{NCer} < 50\%$, and its absence above $X_{NCer} > 50\%$. The presence of fluid obscures the pretransition, giving rise to modest changes in the photophysical parameters of the probes, compared with the main transition. However, by replotting the data as a function of $X_{NCer}$ for each temperature (as exemplified in the Supplementary Material, Fig. S1), it was possible to determine the point at which only $G_m$ is present. This was detected by TMA-DPH, and corresponds to the $X_{NCer}$ where anisotropy reaches a plateau. For up to 22°C, the concentration of NCer required to attain this plateau is always close to 50%, suggesting the presence of an almost vertical boundary (*L5*,

Fig. 7) in the diagram that separates the $G_m$ phase from the $G_m + F$ coexistence region, on the right and left sides of the boundary, respectively. The presence of this coexistence region can be clearly concluded from the linear trend of variation of TMA-DPH anisotropy (Fig. S1). In addition, thermodynamic restrictions dictate that only one phase can change within two adjacent regions (64), and below and above a horizontal line, two phases must be present. This rule further implies that on the right side of L5, a small region of gel-gel coexistence ($G_m + G_p$) must be present (separated by *L4* and *L6*, Fig. 7), so that the diagram has thermodynamic consistency. This region is very narrow, as observed in other phase diagrams for fluid mixtures with peritectic behavior (62). These boundaries (L4, L5, and L6) are further confirmed by x-ray data: for 50% NCer, SAXS shows a sharp and relatively narrow peak at $d \sim 61.5$ Å, whereas at 80% NCer, the peak is very broad and indicative of gel-gel coexistence. Two peaks in the hexagonal packing region appear in the WAXS. In addition, the data show that the contribution of the fluid phase decreases with an increase in NCer content, because the WAXS reflection attributed to the fluid phase disappears, and the lamellar distance increases. In fact, upon crossing the L5 boundary, i.e., for 60% NCer, the repeat distance decreases to a value similar to that obtained for pure NCer, showing that no fluid phase is present.

The phase diagram in Fig. 7 is the simplest one consistent with both the experimental data and thermodynamic restrictions. Still, it is not unlikely that other phases and phase coexistence regions exist for these mixtures. For instance, DSC thermograms of mixtures containing a high NCer molar fraction exhibit an additional transition at higher temperatures (Fig. 3). Because this transition occurs under conditions very far from physiological, and exerts no interference on with the main boundaries of the diagram, its nature was not further investigated. However, it is likely to correspond to a transition to a nonlamellar phase because of the strong tendency of long-chain Cer to promote the formation of hexagonal phases (29). For instance, for NCer >70% and at T > $T_m$, the liquidus boundary (L1) is almost horizontal, and thus another coexistence region could be present, e.g., a coexistence region similar to the one proposed for POPC/PCer mixtures (10), or a region of coexistence of a hexagonal with a lamellar phase.

Based on the phase diagram, the existence of a large gel/ fluid coexistence region reflecting the nonideality and immiscibility of the two lipids is evident. The phase diagram highlights the fact that between room temperature (24°C) and physiological temperature (37°C), the stable phases include the fluid and the partial interdigitated gel, forming for $X_{NCer}$ ~25% at 37°C.

## CONCLUSIONS

The complexity in the phase behavior of POPC/NCer binary mixtures is a result of the marked structural dissimilarities between these lipids. The study of this system in the complete

composition range, together with the microscopic morphological study for selected compositions, was important for understanding POPC/NCer interactions, and for assigning lipid phases. Moreover, it was necessary to determine how NCer affects a fluid bilayer fully hydrated at 37°C. This is because it is difficult to predict what kind of behavior should have the system of an asymmetric phospholipid such as POPC, with a saturated and monounsaturated chain, mixed with an even more asymmetric lipid, with a sphingoid base that matches approximately the POPC chain, but also has a very small headgroup, and furthermore a very long acyl chain that presents an unsaturation.

Systematic and thermodynamic studies of mixtures of highly asymmetric lipids with different headgroups are far from abundant. Here we show that despite its high complexity, the system can be accurately described with a peritectic phase diagram similar to the iron-carbon mixture (64). The phase diagram is characterized by several regions presenting phase separations, both gel-fluid and gel-gel. Nervonoylceramide presents a relatively low solubility in fluid POPC, leading to a broad region of $G_p + F$ coexistence. For comparison, the liquidus and solidus predicted for this mixture, in case it behaved ideally, are also shown in the phase diagram (*IM 1* and *IM 2*, respectively, in Fig. 7). These boundaries were calculated using $\Delta H_{POPC} = 5.8$ kcal/mol (35) and $\Delta H_{Gal-NCer} = 7$ kcal/mol (46). It can be seen that the real $G_p + F$ region is much broader than it would be if the system behaved ideally. Importantly, the deviation from the ideality is more pronounced in the region of low NCer fractions. Nevertheless, compared with other long-chain Cer, e.g., PCer (10), the NCer solubility in fluid is higher. For example, 10% and 30% NCer are required to drive gel-fluid phase separation at 24°C and 37°C, respectively. Similar observations were made for DMPC/PCer and DMPC/NCer mixtures (19). In addition, for very high NCer concentrations, the liquidus and solidus boundaries (L1 and L2, respectively) are quite close to ideality. The similarity between the experimental solidus boundaries and ideal mixing suggests that $\Delta H$ for NCer should be slightly lower than the one used (Gal-NCer), because the entire diagram suggests strong deviation from the ideality, and the DSC scans indicate a low $\Delta H$ for NCer.

Also interesting is the ability of NCer to form interdigitated gel phases that can segregate into tubular structures, making this lipid a good candidate in the modulation of biological processes such as: 1), signal transduction across membrane leaflets; 2), membrane fusion, fission, and budding; and 3), sorting of lipids and proteins, or even morphological specializations that occur, e.g., in neural cells which are enriched in C24:1 sphingolipids.

On the other hand, if the formation of Cer gel domains is required for the activation of signaling cascades that lead to apoptosis, then NCer is probably a worse candidate than PCer for apoptosis induction, because higher levels of NCer are needed for gel-domain formation (10). The distinct biophysical behavior of different Cer again raises the question (or hypothesis) of a requirement for a certain Cer to modulate a specific biological process, as previously suggested for the differential expression of ceramide synthase genes (65).

## SUPPLEMENTARY MATERIAL

To view all of the supplemental files associated with this article, visit www.biophysj.org.

## REFERENCES

1. Merrill, A. H. 2002. De novo sphingolipid biosynthesis: a necessary, but dangerous, pathway. *J. Biol. Chem.* 277:25843–25846.

2. Ohanian, J., and V. Ohanian. 2001. Sphingolipids in mammalian cell signalling. *Cell. Mol. Life Sci.* 58:2053–2068.

3. Zheng, W., J. Kollmeyer, H. Symolon, A. Momin, E. Munter, E. Wang, S. Kelly, J. C. Allegood, Y. Liu, Q. Peng, H. Ramaraju, M. C. Sullards, M. Cabot, and A. H. Merrill. 2006. Ceramides and other bioactive sphingolipid backbones in health and disease: lipidomic analysis, metabolism and roles in membrane structure, dynamics, signaling and autophagy. *Biochim. Biophys. Acta.* 1758:1864–1884.

4. Taha, T. A., T. D. Mullen, and L. M. Obeid. 2006. A house divided: ceramide, sphingosine, and sphingosine-1-phosphate in programmed cell death. *Biochim. Biophys. Acta.* 1758:2027–2036.

5. Fahy, E., S. Subramaniam, H. A. Brown, C. K. Glass, A. H. Merrill, R. C. Murphy, C. R. H. Raetz, D. W. Russell, Y. Seyama, W. Shaw, T. Shimizu, F. Spener, G. van Meer, M. S. VanNieuwenhze, S. H. White, J. L. Witztum, and E. A. Dennis. 2005. A comprehensive classification system for lipids. *J. Lipid Res.* 46:839–861.

6. Goni, F. M., F. X. Contreras, L. R. Montes, J. Sot, and A. Alonso. 2005. Biophysics (and sociology) of ceramides. *Biochem. Soc. Symp.* 72:177–188.

7. Futerman, A. H., and Y. A. Hannun. 2004. The complex life of simple sphingolipids. *EMBO Rep.* 5:777–782.

8. Schenck, M., A. Carpinteiro, H. Grassme, F. Lang, and E. Gulbins. 2007. Ceramide: physiological and pathophysiological aspects. *Arch. Biochem. Biophys.* 462:171–175.

9. Hsueh, Y. W., R. Giles, N. Kitson, and J. Thewalt. 2002. The effect of ceramide on phosphatidylcholine membranes: a deuterium NMR study. *Biophys. J.* 82:3089–3095.

10. Silva, L., R. F. M. De Almeida, A. Fedorov, A. P. A. Matos, and M. Prieto. 2006. Ceramide-platform formation and -induced biophysical changes in a fluid phospholipid membrane. *Mol. Membr. Biol.* 23:137–150.

11. Siskind, L. J., R. N. Kolesnick, and M. Colombini. 2006. Ceramide forms channels in mitochondrial outer membranes at physiologically relevant concentrations. *Mitochondrion.* 6:118–125.

12. Contreras, F. X., A. V. Villar, A. Alonso, R. N. Kolesnick, and F. M. Goñi. 2003. Sphingomyelinase activity causes transbilayer lipid translocation in model and cell membranes. *J. Biol. Chem.* 278:37169–37174.

13. Contreras, F. X., G. Basanez, A. Alonso, A. Herrmann, and F. M. Goñi. 2005. Asymmetric addition of ceramides but not dihydroceramides promotes transbilayer (flip-flop) lipid motion in membranes. *Biophys. J.* 88:348–359.

14. Carrer, D. C., and B. Maggio. 1999. Phase behavior and molecular interactions in mixtures of ceramide with dipalmitoylphosphatidylcholine. *J. Lipid Res.* 40:1978–1989.

15. Holopainen, J. M., J. Y. A. Lehtonen, and P. K. J. Kinnunen. 1997. Lipid microdomains in dimyristoylphosphatidylcholine—ceramide liposomes. *Chem. Phys. Lipids.* 88:1–13.

16. Holopainen, J. M., J. Lemmich, F. Richter, O. G. Mouritsen, G. Rapp, and P. K. J. Kinnunen. 2000. Dimyristoylphosphatidylcholine/C16:0-ceramide binary liposomes studied by differential scanning calorimetry and wide- and small-angle x-ray scattering. *Biophys. J.* 78:2459–2469.

17. Silva, L. C., R. F. M. De Almeida, B. M. Castro, A. Fedorov, and M. Prieto. 2007. Ceramide-domain formation and collapse in lipid rafts: Membrane reorganization by an apoptotic lipid. *Biophys. J.* 92:502–516.

18. Castro, B. M., R. F. M. De Almeida, L. C. Silva, A. Fedorov, and M. Prieto. 2007. Formation of ceramide/sphingomyelin gel domains in the presence of an unsaturated phospholipid: a quantitative multiprobe approach. *Biophys. J.* 93:1639–1650.

19. Holopainen, J. M., H. L. Brockman, R. E. Brown, and P. K. J. Kinnunen. 2001. Interfacial interactions of ceramide with dimyristoyl-phosphatidylcholine: impact of the *N*-acyl chain. *Biophys. J.* 80:765–775.

20. Carrer, D. C., S. Härtel, H. L. Monaco, and B. Maggio. 2003. Ceramide modulates the lipid membrane organization at molecular and supra-molecular levels. *Chem. Phys. Lipids.* 122:147–152.

21. Laviad, E. L., L. Albee, I. Pankova-Kholmyansky, S. Epstein, H. Park, A. H. Merrill, and A. H. Futerman. 2008. Characterization of ceramide synthase 2—tissue distribution, substrate specificity, and inhibition by sphingosine 1-phosphate. *J. Biol. Chem.* 283:5677–5684.

22. Huang, C. H., and J. T. Mason. 1986. Structure and properties of mixed-chain phospholipid assemblies. *Biochim. Biophys. Acta.* 864:423–470.

23. Putzel, G. G., and M. Schick. 2008. Phase behavior of a model bilayer membrane with coupled leaves. *Biophys. J.* 94:869–877.

24. Vierl, U., L. Lobbecke, N. Nagel, and G. Cevc. 1994. Solute effects on the colloidal and phase-behavior of lipid bilayer-membranes—ethanol-dipalmitoylphosphatidylcholine mixtures. *Biophys. J.* 67:1067–1079.

25. Sklar, L. A., B. S. Hudson, M. Petersen, and J. Diamond. 1977. Conjugated polyene fatty-acids on fluorescent-probes—spectroscopic characterization. *Biochemistry.* 16:813–819.

26. Lentz, B. 1988. Membrane ''fluidity'' from fluorescence anisotropy measurements. *In* Spectroscopic Membrane Probes, Vol. I. L. Loew, editor. CRC, Boca Raton, FL. 13–41.

27. De Almeida, R. F. M., A. Fedorov, and M. Prieto. 2003. Sphingo-myelin/phosphatidylcholine/cholesterol phase diagram: boundaries and composition of lipid rafts. *Biophys. J.* 85:2406–2416.

28. De Almeida, R. F. M., L. M. S. Loura, A. Fedorov, and M. Prieto. 2005. Lipid rafts have different sizes depending on membrane composition: a time-resolved fluorescence resonance energy transfer study. *J. Mol. Biol.* 346:1109–1120.

29. Veiga, M. P., J. L. R. Arrondo, F. M. Goni, and A. Alonso. 1999. Ceramides in phospholipid membranes: effects on bilayer stability and transition to nonlamellar phases. *Biophys. J.* 76:342–350.

30. De Almeida, R. F. M., J. Borst, A. Fedorov, M. Prieto, and A. J. W. G. Visser. 2007. Complexity of lipid domains and rafts in giant uni-lamellar vesicles revealed by combining imaging and microscopic and macroscopic time-resolved fluorescence. *Biophys. J.* 93:539–553.

31. Ayuyan, A. G., and F. S. Cohen. 2006. Lipid peroxides promote large rafts: effects of excitation of probes in fluorescence microscopy and electrochemical reactions during vesicle formation. *Biophys. J.* 91:2172–2183.

32. Sot, J., L. A. Bagatolli, F. M. Goñi, and A. Alonso. 2006. Detergent-resistant, ceramide-enriched domains in sphingomyelin/ceramide bilayers. *Biophys. J.* 90:903–914.

33. Metso, A. J., H. X. Zhao, K. Tuunainen, and P. K. J. Kinnunen. 2005. Observation of the main phase transition of dinervonoylphosphocho-line giant liposomes by fluorescence microscopy. *Biochim. Biophys. Acta.* 1713:83–91.

34. Levin, I. W., T. E. Thompson, Y. Barenholz, and C. Huang. 1985. Two types of hydrocarbon chain interdigitation in sphingomyelin bilayers. *Biochemistry.* 24:6282–6286.

35. Koynova, R., and M. Caffrey. 1998. Phases and phase transitions of the phosphatidylcholines. *Biochim. Biophys. Acta.* 1376:91–145.

36. Sklar, L. A., G. P. Miljanich, and E. A. Dratz. 1979. Phospholipid lateral phase separation and the partition of cis-parinaric acid and trans-parinaric acid among aqueous, solid lipid, and fluid lipid phases. *Biochemistry.* 18:1707–1716.

37. Lakowicz, J. 1999. Principles of Fluorescence Spectroscopy. Kluwer Academics, New York.

38. Parente, R. A., and B. R. Lentz. 1985. Advantages and limitations of 1-palmitoyl-2-[[2-[4-(6-phenyl-trans-1,3,5-hexatrienyl)phenyl]eth-yl]carb onyl]-3-Sn-phosphatidylcholine as a fluorescent membrane probe. *Biochemistry.* 24:6178–6185.

39. Mcintosh, T. J., S. A. Simon, J. C. Ellington, and N. A. Porter. 1984. New structural model for mixed-chain phosphatidylcholine bilayers. *Biochemistry.* 23:4038–4044.

40. Lewis, R. N., R. N. McElhaney, F. Osterberg, and S. M. Gruner. 1994. Enigmatic thermotropic phase behavior of highly asymmetric mixed-chain phosphatidylcholines that form mixed-interdigitated gel phases. *Biophys. J.* 66:207–216.

41. Shah, J., J. M. Atienza, A. V. Rawlings, and G. G. Shipley. 1995. Physical-properties of ceramides—effect of fatty-acid hydroxylation. *J. Lipid Res.* 36:1945–1955.

42. Fidorra, M., L. Duelund, C. Leidy, A. C. Simonsen, and L. A. Bagatolli. 2006. Absence of fluid-ordered/fluid-disordered phase coexistence in ceramide/ POPC mixtures containing cholesterol. *Biophys. J.* 90:4437–4451.

43. Shah, J., J. M. Atienza, R. I. Duclos, A. V. Rawlings, Z. X. Dong, and G. G. Shipley. 1995. Structural and thermotropic properties of synthetic C16–0 (palmitoyl) ceramide—effect of hydration. *J. Lipid Res.* 36:1936–1944.

44. Chen, H. C., R. Mendelsohn, M. E. Rerek, and D. J. Moore. 2000. Fourier transform infrared spectroscopy and differential scanning calorimetry studies of fatty acid homogeneous ceramide 2. *Biochim. Biophys. Acta.* 1468:293–303.

45. Li, X. M., J. M. Smaby, M. M. Momsen, H. L. Brockman, and R. E. Brown. 2000. Sphingomyelin interfacial behavior: the impact of changing acyl chain composition. *Biophys. J.* 78:1921–1931.

46. Kulkarni, V. S., W. H. Anderson, and R. E. Brown. 1995. Bilayer nanotubes and helical ribbons formed by hydrated galactosylcer-amides: acyl chain and headgroup effects. *Biophys. J.* 69:1976–1986.

47. Robert, B. Gennis. 1989. Biomembranes Molecular Structure and Function. New York.

48. Niemela, P. S., M. T. Hyvonen, and I. Vattulainen. 2006. Influence of chain length and unsaturation on sphingomyelin bilayers. *Biophys. J.* 90:851–863.

49. Boggs, J. M. 1987. Lipid intermolecular hydrogen-bonding—influence on structural organization and membrane-function. *Biochim. Biophys. Acta.* 906:353–404.

50. Ramstedt, B., and J. P. Slotte. 2006. Sphingolipids and the formation of sterol-enriched ordered membrane domains. *Biochim. Biophys. Acta.* 1758:1945–1956.

51. Saxena, K., R. I. Duclos, P. Zimmermann, R. R. Schmidt, and G. G. Shipley. 1999. Structure and properties of totally synthetic galacto- and gluco-cerebrosides. *J. Lipid Res.* 40:839–849.

52. Carrer, D. C., S. Schreier, M. Patrito, and B. Maggio. 2006. Effects of a short-chain ceramide on bilayer domain formation, thickness, and chain mobility: DMPC and asymmetric ceramide mixtures. *Biophys. J.* 90:2394–2403.

53. Reed, R. A., and G. G. Shipley. 1987. Structure and metastability of *N*-lignocerylgalactosylsphingosine (cerebroside) bilayers. *Biochim. Biophys. Acta.* 896:153–164.

54. Takahashi, H., T. Hayakawa, Y. Kawasaki, K. Ito, T. Fujisawa, M. Kodama, and T. Kobayashi. 2007. Structural characterization of *N*-lignoceroyl (C24:0) sphingomyelin bilayer membranes: a re-evaluation. *J. Appl. Cryst.* 40:s312–s317.

55. Mason, J. T., C. H. Huang, and R. L. Biltonen. 1981. Calorimetric investigations of saturated mixed-chain phosphatidylcholine bilayer dispersions. *Biochemistry.* 20:6086–6092.

56. Huang, C. 1990. Mixed-chain phospholipids and interdigitated bilayer systems. *Klin. Wochenschr.* 68:149–165.

57. Li, S., Z. Q. Wang, H. N. Lin, and C. Huang. 1993. Energy-minimized structures and packing states of a homologous series of mixed-chain phosphatidylcholines: a molecular mechanics study on the diglyceride moieties. *Biophys. J.* 65:1415–1428.

58. Goldstein, A. S., A. N. Lukyanov, P. A. Carlson, P. Yager, and M. H. Gelb. 1997. Formation of high-axial-ratio-microstructures from natural and synthetic sphingolipids. *Chem. Phys. Lipids.* 88:21–36.

59. Kulkarni, V. S., J. M. Boggs, and R. E. Brown. 1999. Modulation of nanotube formation by structural modifications of sphingolipids. *Biophys. J.* 77:319–330.

60. Hannun, Y. A. 1996. Functions of ceramide in coordinating cellular responses to stress. *Science.* 274:1855–1859.

61. Gutberlet, T., U. Dietrich, G. Klose, and G. Rapp. 1998. X-ray diffraction study of the lamellar-hexagonal phase transition in phospholipid/surfactant mixtures. *J. Colloid Interface Sci.* 203:317–327.

62. Marsh, D. 1990. Handbook of Lipid Bilayers. CRC Press, Boca Raton, FL.

63. Mabrey, S., and J. M. Sturtevant. 1976. Investigation of phase transitions of lipids and lipid mixtures by high sensitivity differential scanning calorimetry. *Proc. Natl. Acad. Sci. USA.* 73:3862–3866.

64. Rhines, F. N. 1956. Phase Diagrams in Metallurgy: Their Development and Application. McGraw-Hill, New York.

65. Pewzner-Jung, Y., S. Ben Dor, and A. H. Futerman. 2006. When do lasses (longevity assurance genes) become CerS (ceramide synthases)? Insights into the regulation of ceramide synthesis. *J. Biol. Chem.* 281: 25001–25005.